The effect of baryons on the inner density profiles of rich clusters

Matthieu Schaller,[1]⋆ Carlos S. Frenk,[1] Richard G. Bower,[1] Tom Theuns,[1] James Trayford,[1] Robert A. Crain,[2,3] Michelle Furlong,[1] Joop Schaye,[2] Claudio Dalla Vecchia[4,5] and I. G. McCarthy[3]

[1]*Institute for Computational Cosmology, Durham University, South Road, Durham DH1 3LE, UK*
[2]*Leiden Observatory, Leiden University, PO Box 9513, NL-2300 RA Leiden, the Netherlands*
[3]*Astrophysics Research Institute, Liverpool John Moores University, 146 Brownlow Hill, Liverpool L3 5RF, UK*
[4]*Instituto de Astrofísica de Canarias, C/ Vía Láctea s/n, E-38205 La Laguna, Tenerife, Spain*
[5]*Departamento de Astrofísica, Universidad de La Laguna Av. del Astrofísico Franciso Sánchez s/n, E-38206 La Laguna, Tenerife, Spain*

ABSTRACT

We use the 'Evolution and assembly of galaxies and their environments' (EAGLE) cosmological simulation to investigate the effect of baryons on the density profiles of rich galaxy clusters. We focus on EAGLE clusters with $M_{200} > 10^{14} \, M_{\odot}$ of which we have six examples. The central brightest cluster galaxies (BCGs) in the simulation have steep stellar density profiles, $\rho_*(r) \propto r^{-3}$. Stars dominate the mass density for $r < 10$ kpc, and, as a result, the *total* mass density profiles are steeper than the Navarro–Frenk–White (NFW) profile, in remarkable agreement with observations. The dark matter halo itself closely follows the NFW form at all resolved radii ($r \gtrsim 3.0$ kpc). The EAGLE BCGs have similar surface brightness and line-of-sight velocity dispersion profiles as the BCGs in the sample of Newman et al., which have the most detailed measurements currently available. After subtracting the contribution of the stars to the central density, Newman et al. infer significantly shallower slopes than the NFW value, in contradiction with the EAGLE results. We discuss possible reasons for this discrepancy, and conclude that an inconsistency between the kinematical model adopted by Newman et al. for their BCGs, which assumes isotropic stellar orbits, and the kinematical structure of the EAGLE BCGs, in which the orbital stellar anisotropy varies with radius and tends to be radially biased, could explain at least part of the discrepancy.

Key words: galaxies: clusters: general – galaxies: haloes – cosmology: theory – dark matter.

1 INTRODUCTION

Simulations of structure formation in the cold dark matter (CDM) model predict that relaxed dark matter (DM) haloes of all masses should have nearly self-similar spherically-averaged density profiles that are well described by a simple law with a central cusp, $\rho(r) \propto r^{-1}$, and a steeper slope, $\rho(r) \propto r^{-3}$, at large radii (Navarro, Frenk & White 1996b, 1997). This Navarro–Frenk–White (NFW) profile provides a good approximation to haloes in *N*-body simulations, in which the DM is treated as a collisionless fluid. Very high resolution simulations of this kind have shown that the profiles are not always completely self-similar and that the inner slope could be shallower than the asymptotic NFW value (Navarro et al. 2004, 2010; Neto et al. 2007; Gao et al. 2008, 2012; Dutton & Macciò

2014). Despite these small variations, the form of the DM density profile is a robust and testable prediction of the CDM paradigm.

In the real world sufficiently massive haloes contain baryons whose evolution might affect the density structure of the DM. Several processes have been proposed that could modify the central density profile, flattening it (Navarro, Eke & Frenk 1996a; Pontzen & Governato 2012; Martizzi et al. 2012) steepening it (Blumenthal et al. 1986; Gnedin et al. 2004) or leaving it broadly unchanged (Laporte & White 2014). Understanding the impact of these competing effects requires cosmological hydrodynamical simulations (e.g. Duffy et al. 2010; Gnedin et al. 2011; Di Cintio et al. 2014; Vogelsberger et al. 2014), but these are far more challenging than *N*-body simulations and it is still unclear whether they can treat all the relevant scales and processes sufficiently accurately.

If the effects of baryons can be reliably established, the density profiles of haloes could, in principle, reveal much about the nature of the DM. For example, if the dark were self-interacting rather than effectively collisionless, with a sufficiently large self-interaction

⋆ E-mail: matthieu.schaller@durham.ac.uk

cross-section, the inner halo density profile could be shallower than the NFW form even in the absence of baryonic effects (e.g. Spergel & Steinhardt 2000; Vogelsberger, Zavala & Loeb 2012; Rocha et al. 2013). Similarly, if DM particles decay or annihilate, they could produce potentially detectable particles or radiation whose intensity depends sensitively on the inner density profile.

From the observational point of view, studies of the inner DM density profiles have focused on the two extremes of the halo mass distribution: dwarf galaxies and galaxy clusters. Dwarf galaxies (e.g. Walker & Penarrubia 2011) are attractive because their very high mass-to-light ratios suggest that baryonic effects may have been unimportant. However, degeneracies in the analysis of photometric and kinematic data have so far led to inconclusive results (e.g. Strigari, Frenk & White 2010, 2014). Galaxy clusters are also attractive because baryons are relatively less important in the central regions than in L_* galaxies and their inner profiles can be probed by strong and weak lensing, as well as by the stellar kinematics of the central cluster galaxy.

Studies of the inner DM density structure in clusters have so far produced conflicting results. For example, Okabe et al. (2013) find that a sample of 50 clusters with good gravitational lensing data have density profiles that agree well with the NFW form from the inner $100h^{-1}$ kpc to the virial radius. Using X-ray observations, Pointecouteau, Arnaud & Pratt (2005), Vikhlinin et al. (2006) and Umetsu et al. (2014) similarly find that the total matter profile follows closely an NFW profile at $r \gtrsim 0.05R_{200} \approx 10\text{-}20$ kpc. On the other hand, combining strong and weak lensing with stellar kinematics, Sand et al. (2004) and Newman et al. (2013a,b) find that the total central profile closely follows the NFW form but, once the contribution of the stellar component has been subtracted, the inferred DM density profile is significantly flatter than NFW.

Here we analyse a sample of massive clusters ($M_{200} \gtrsim 10^{14}$ M$_\odot$) from the 'Evolution and assembly of galaxies and their environment' (EAGLE) cosmological hydrodynamical simulation (Crain et al. 2015; Schaye et al. 2015). This is one of a new generation of simulations which follow the evolution of relatively large volumes using the best current understanding of the physical processes responsible for galaxy formation. Since many of these processes cannot be resolved in these simulations, they are represented by 'subgrid' models which can be quite different in different simulations (e.g. Schaye et al. 2010; Scannapieco et al. 2012; Okamoto, Shimizu & Yoshida 2014; Vogelsberger et al. 2014).

The EAGLE simulation is sufficiently realistic that it may be compared to a range of observed galaxy properties at different cosmic epochs. The galaxy population in the simulation shows broad agreement with basic properties such as the stellar mass function and star formation history, colour, size and morphology distributions, as well as scaling relations between photometric and structural properties (Crain et al. 2015; Furlong et al. 2015; Schaye et al. 2015; Trayford et al. 2015). In this paper we focus on the effects of baryonic processes on the central density structure of the most massive galaxy clusters in the EAGLE simulation.

Our paper is organized as follows: in Section 2, we briefly describe the EAGLE simulation; in Section 3, we measure the density profile of our simulated clusters; in Section 4 we focus on the inner profile slope and compare to recent observations; in Section 5, we carry out a more detailed comparison with the data of Newman et al. (2013b). We summarize our results in Section 6. Throughout this paper, we assume values of the cosmological parameters inferred from the *Planck* satellite data for a ΛCDM cosmology (Planck Collaboration XVI 2014), the most relevant of which are Hubble constant, $H_0 = 67.7$ km s^{-1} Mpc^{-1}; baryon and total matter densi-

ties in units of the critical density, $\Omega_b = 0.0482$ and $\Omega_m = 0.307$, respectively, and linear power spectrum normalization, $\sigma_8 = 0.829$.

2 THE EAGLE SIMULATIONS

The EAGLE set consists of a series of cosmological simulations with state-of-the-art treatments of smoothed particle hydrodynamics and subgrid models. The simulations reproduce the stellar mass function and other observed properties of the galaxy population at $z = 0$, and produce a reasonable evolution of the main observed galaxy properties over cosmic time (Crain et al. 2015; Furlong et al. 2015; Schaye et al. 2015).

In brief, the largest EAGLE simulation follows $1504^3 \approx 3.4 \times 10^9$ DM particles and the same number of gas particles in a 100^3 Mpc^3 cubic volume[1] from ΛCDM initial conditions generated using second-order Lagrangian perturbation theory (Jenkins 2010) with the linear phases taken from the public multiscale Gaussian white noise field, PANPHASIA (Jenkins 2013). The mass of a DM particle is 9.7×10^6 M$_\odot$ and the initial mass of a gas particle is 1.8×10^6 M$_\odot$. The gravitational softening length is 700 pc (Plummer equivalent). The simulation was performed with a heavily modified version of the GADGET-3 code last described by Springel (2005), using a pressure-entropy formulation of SPH (Hopkins 2013) and new prescriptions for viscosity and thermal diffusion (Dalla Vecchia, in preparation; Schaller et al., in preparation) and time stepping (Durier & Dalla Vecchia 2012). We now summarize the subgrid model.

2.1 Baryon physics

The subgrid model is an improved version of that used in the GIMIC and OWLS simulations (Crain et al. 2009; Schaye et al. 2010). Star formation is implemented using a pressure-dependant prescription that reproduces the observed Kennicutt–Schmidt star formation law (Schaye & Dalla Vecchia 2008) and uses a threshold that captures the metallicity dependence of the transition from the warm, atomic to the cold, molecular gas phase (Schaye 2004). Star particles are treated as single stellar populations (SSPs) with a Chabrier (2003) initial mass function (IMF) evolving along the tracks provided by Portinari, Chiosi & Bressan (1998). Metals from asymptotic giant branch stars and supernovae (SNe) are injected into the interstellar medium (ISM) following the prescriptions of Wiersma et al. (2009b) and stellar feedback is implemented by injecting thermal energy into the gas as described in Dalla Vecchia & Schaye (2012). The amount of energy injected into the ISM by SNe is assumed to depend on the local gas metallicity and density in an attempt to take into account the unresolved structure of the ISM (Schaye et al. 2015). Supermassive black hole seeds are injected in haloes above $10^{10} h^{-1}$ M$_\odot$ and grow through mergers and accretion of low angular momentum gas (Rosas-Guevara et al. 2013; Schaye et al. 2015). AGN feedback is modelled by the injection of thermal energy into the gas surrounding the black hole (Booth & Schaye 2009; Dalla Vecchia & Schaye 2012).

The subgrid model was calibrated (mostly by adjusting the intensity of stellar feedback and the accretion rate on to black holes) so as to reproduce the present day stellar mass function and galaxy sizes (Crain et al. 2015). The cooling of gas and the interaction with the background radiation is implemented following Wiersma, Schaye & Smith (2009a) who tabulate cooling and photoheating

---

[1] Note that the units do not have factors of *h*.

rates element-by-element in the presence of UV and X-ray backgrounds (Haardt & Madau 2001).

Haloes were identified using the Friends-of-Friends algorithm (Davis et al. 1985) and bound structures within them were then identified using the SUBFIND code (Springel et al. 2001; Dolag et al. 2009). A sphere centred at the minimum of the gravitational potential of each subhalo is grown until the mass contained within a given radius, R_{200}, reaches $M_{200} = 200 \left(4\pi\rho_{cr}(z)R_{200}^3/3\right)$, where $\rho_{cr}(z) = 3H(z)^2/8\pi G$ is the critical density at the redshift of interest.

2.2 Photometry

The luminosity and surface brightness of galaxies in the simulation are computed on a particle-by-particle basis as described by Trayford et al. (2015). The basic prescription for deriving the photometric attributes of each star particle is as follows. Each star particle is treated as a SSP of the appropriate age and metallicity as given by the simulation. The Bruzual & Charlot (2003, hereafter BC03) population synthesis model (assuming a Chabrier (2003) IMF for consistency with the simulation) gives the integrated spectrum of an SSP on a grid of age and metallicity. Using bilinear interpolation we estimate the radiated power in a particular band by integrating the spectrum through a filter transmission curve. (Before assigning broad-band luminosities, the metallicities are renormalized so that solar metallicity ($Z_\odot = 0.012$) is consistent with the older solar value assumed by BC03 ($Z_\odot = 0.02$).)

Because of the limited resolution of the simulation, a star particle represents a relatively large stellar mass. To mitigate discreteness effects, in each star formation event star particles with stellar ages <100 Myr are resampled from their progenitor gas particles and the currently star-forming gas in the subhalo in which the particle resides. Such resampling improves the match to the observed bimodality in galaxy colour–magnitude diagrams (Trayford et al. 2015). However, this treatment has very little impact on the properties of the brightest cluster galaxies (BCGs) of interest here as their current star formation rates are negligible.

A modified Charlot & Fall (2000) dust model is used to attenuate the light emitted by star particles. The extinction is computed using a constant ISM optical depth and a transient molecular cloud component that disperses after 10 Myr. We modified the model so that these values scale proportionally with galaxy metallicity according to the observed mass–metallicity relation of Tremonti et al. (2004). The resulting galaxy population gives a very good match to the observed luminosity function in various commonly used broad-bands (Trayford et al. 2015).

3 THE MASS DENSITY PROFILE OF CLUSTERS

Our cluster sample consists of the six EAGLE haloes of mass $M_{200} > 10^{14}$ M$_\odot$ (see Table 1), which we label Clusters 1 to 6. These clusters have moderate sphericity and would likely be considered relaxed in observational studies even if some of them fail the strict relaxation criteria used in simulations (Neto et al. 2007). The stellar mass function of our cluster galaxies (including the BCG) provides a good match to observations. Similarly, the sizes of cluster galaxies are in good agreement with observations. Thus, in many respects, the EAGLE rich cluster sample is quite realistic. It is worth mentioning that Schaye et al. (2015) showed that the gas fractions within R_{500} of the clusters in our sample may be too high when compared to observations. However, this small disagreement does not affect the

Table 1. Properties of the six simulated clusters studied in this work. The stellar mass is measured within a 30 kpc spherical aperture. The baryon and stellar fractions are measured within R_{200} and are given in units of the universal baryon fraction, $f_b^{univ} = \Omega_b/\Omega_m = 0.157$.

| Halo	M_{200} (M$_\odot$)	R_{200} (kpc)	M_* (M$_\odot$)	f_b/f_b^{univ}	f_*/f_b^{univ}
1	1.9×10^{14}	1206	4.2×10^{11}	0.99	0.07
2	3.7×10^{14}	1518	3.5×10^{11}	0.94	0.08
3	3.0×10^{14}	1411	2.9×10^{11}	0.95	0.08
4	3.1×10^{14}	1422	4.5×10^{11}	0.97	0.07
5	2.0×10^{14}	1225	2.0×10^{11}	0.92	0.08
6	2.0×10^{14}	1229	3.7×10^{11}	0.93	0.08
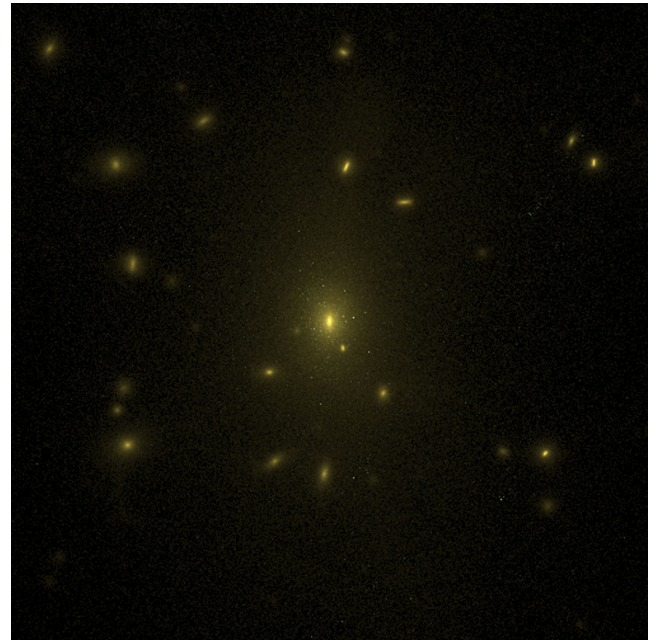
Figure 1. Surface brightness map of Cluster 1, using the SDSS *ugr* filter system. The map is 500 kpc on a side and has resolution of 1 kpc. The central galaxy is easily visible and appears slightly elongated in projection. Satellite galaxies are also visible and cluster around the BCG.

results of this study where we focus on the very centres of the haloes ($r \lesssim 20$ kpc) where the mass of gas is very small (see Fig. 2).

The main properties of our rich cluster sample are listed in Table 1. As shown by Schaye et al. (2015), the galaxy stellar masses are in good agreement with abundance matching relations (Moster, Naab & White 2013). At the same time, the overall gas fractions within R_{200} are close to the cosmic mean, $f_b^{univ} = \Omega_b/\Omega_m$, as observed (Vikhlinin et al. 2006): the AGN feedback model has succeeded in suppressing star formation in the BCG without removing excessive amounts of gas from the haloes.

A surface brightness map of Cluster 1 is shown in Fig. 1. The map is centred on the centre of potential of the halo and shows a 500 kpc × 500 kpc area of sky. Photometry for the model galaxies in the *u*-, *g*- and *r*-band SDSS filters (Doi et al. 2010) was obtained as described in Section 2.2. The surface brightness is then used to construct fake colour mock images following the method of Lupton et al. (2004). As can be seen, the central part of the halo seems spherical. The central galaxy is slightly prolate and the central satellite galaxies cluster around it roughly isotropically.
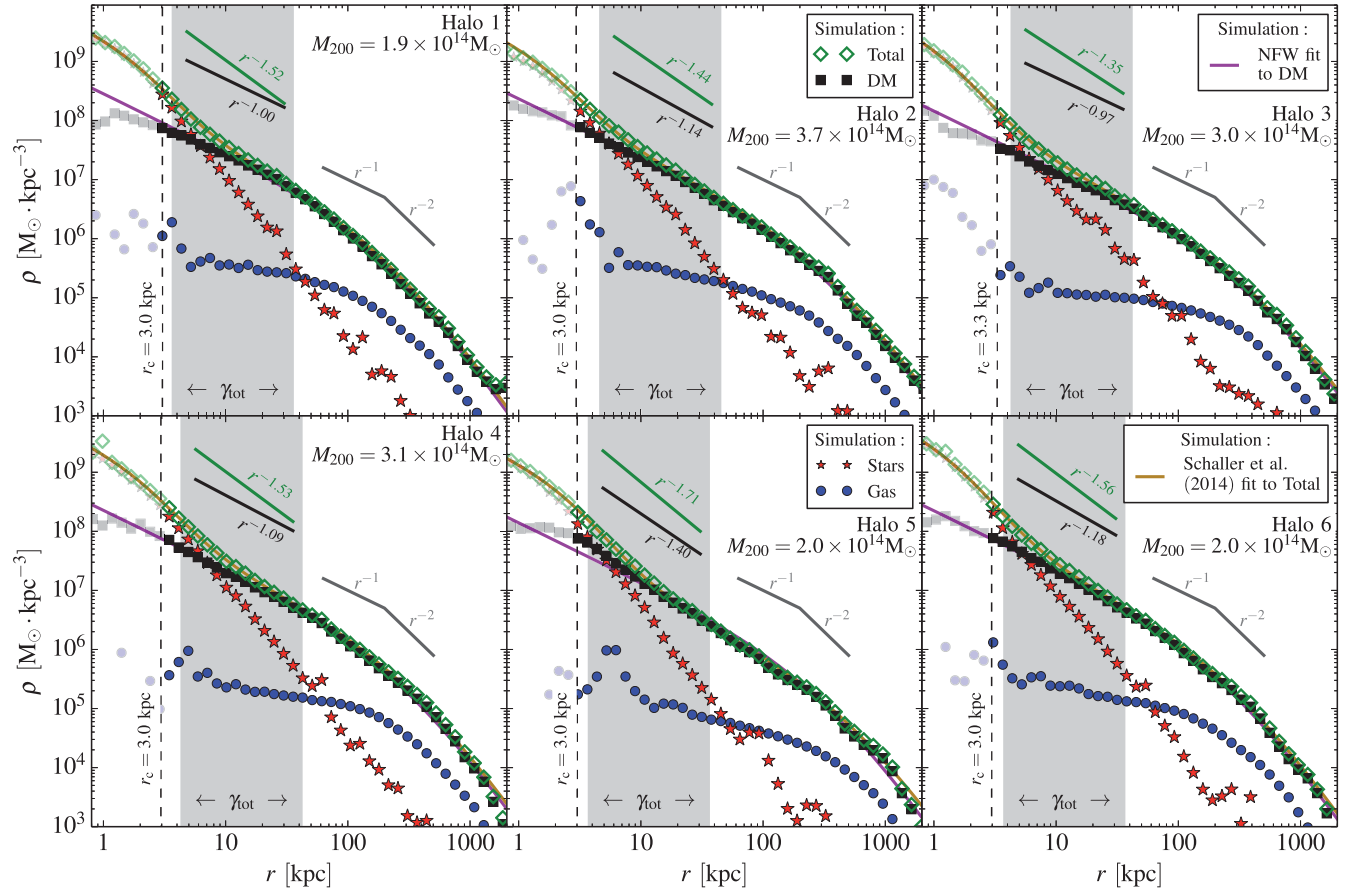
Figure 2. Radial density profiles of the six simulated clusters studied in this paper (see Table 1). Green diamonds represent the total mass profile; the black squares, red stars and blue circles represent the DM, stellar and gas components, respectively. The solid magenta and yellow lines are the best-fitting NFW profile to the DM component and the best-fitting (Schaller et al. 2015) profile (equation 2) to the total mass distribution. The vertical dashed line in each panel shows the convergence radius, r_c, beyond which the density profile has converged to within 20 per cent; data points within this radius are shown by fainter symbols. The grey shaded regions show the radial range over which the logarithmic slopes, γ_{tot} and β_{DM}, of the total and DM profiles are measured. The values of the slopes are given above the simulation points. The DM haloes are very well fitted by NFW profiles and the total mass profiles only deviate from NFW in the central parts ($r \lesssim 10$ kpc), where the stellar component dominates. Note the similarities in the shapes of these six haloes and the relatively small variations that occur mostly in the very central regions.

3.1 The mass density profiles of simulated haloes

To study the density profiles of the EAGLE clusters, we bin the particles in logarithmically spaced radial bins centred on the minimum of the gravitational potential. We measure the DM, gas and stellar components separately and then sum all contributions to obtain the total mass profile. The result is shown in Fig. 2, where the six panels correspond to the six clusters of Table 1. In each panel, the green diamonds, black squares, red stars and blue circles represent the total mass, DM, stellar component and gas, respectively. The mass of each halo is indicated at the top of each panel. The dashed vertical lines show the radius, r_c, above which the profile is considered to have converged within 20 per cent (Power et al. 2003; Schaller et al. 2015). This is a conservative estimate of the convergence radius (~ 3.1 kpc) and it is much larger than the Plummer-equivalent softening length ($\epsilon = 0.7$ kpc) often used as a rough estimate of the radius beyond which numerical effects become unimportant. Data points within this 'convergence radius' but at radii $r > \epsilon$ are shown using fainter symbols.

The DM dominates the density profiles at $r \gtrsim 8$ kpc. At smaller radii, the stellar component dominates and exceeds the DM density by up to an order of magnitude at the centre. The stellar density

profiles are approximatively constant power laws, $r^{-\alpha}$, with $\alpha \approx -3$ down to the very centre of the galaxy. The simulation does not resolve the centre of the BCG and the slopes measured there are probably affected by the force softening (0.7 kpc at $z = 0$) used in the *N*-body solver. The peaks in the stellar components at large radii are caused by satellites orbiting in the halo. The gas is subdominant at all radii, in particular in the central regions where the stellar densities are almost three orders of magnitude higher. The gas only dominates the baryon content at radii $r \gtrsim 50$ kpc. At radii larger than ~ 300 kpc, the gas profile has the same shape as the DM profile. The DM itself has the characteristic NFW shape, whose asymptotic behaviour is a power-law of slope -1 at the centre and a power law of slope -3 in the outer parts.

3.2 Fitting models to the simulated haloes

The density profiles of relaxed DM haloes in *N*-body simulations are well fitted by the near-universal NFW profile which has the form:

$$\frac{\rho(r)}{\rho_{cr}} = \frac{\delta_c}{(r/r_s)(1 + r/r_s)^2} \tag{1}$$

Table 2. Parameters of the best-fitting NFW profiles (equation 1) to the *DM* component of our haloes.

Halo	M_{200} (M$_\odot$)	R_{200} (kpc)	r_s (kpc)	c_{200}	δ_c
1	1.9×10^{14}	1206	199.2	6.1	1.1×10^4
2	3.7×10^{14}	1518	350.8	4.3	5.3×10^3
3	3.0×10^{14}	1411	452.0	3.1	2.5×10^3
4	3.1×10^{14}	1422	305.1	4.7	5.9×10^3
5	2.0×10^{14}	1225	331.1	3.7	3.3×10^3
6	2.0×10^{14}	1229	245.9	5.0	7.2×10^3

Table 3. Parameters of the best-fitting profiles of the form of equation (2) (Schaller et al. 2015) to the *total* matter distribution in our halo sample.

Halo	M_{200} (M$_\odot$)	r_s' (kpc)	δ_c'	r_i (kpc)	δ_i
1	1.9×10^{14}	209.3	1.2×10^4	2.1	8.8×10^6
2	3.7×10^{14}	369.8	5.5×10^3	2.0	6.4×10^6
3	3.0×10^{14}	433.8	3.2×10^3	1.4	1.1×10^7
4	3.1×10^{14}	321.6	6.2×10^3	2.2	7.2×10^6
5	2.0×10^{14}	529.1	1.5×10^3	2.7	4.0×10^6
6	2.0×10^{14}	277.0	6.4×10^3	1.6	1.5×10^7

(Navarro et al. 1996b, 1997), where δ_c is a characteristic amplitude and r_s, a scalelength that is often expressed in terms of the concentration, $c_{200} = R_{200}/r_s$. Both δ_c and c_{200} correlate with halo mass, M_{200}, so the NFW profile is fully specified by the halo mass. In our simulations, the cold gas and stars, which contribute only a small fraction of the total mass, are concentrated towards the centre, while the hot gas beyond the central regions closely follows the DM profile. Thus, even in the presence of baryons, the *DM* still closely follows an NFW profile. In the case of haloes of mass $M_{200} \sim 10^{12}$-10^{13} M$_\odot$, the profile is slightly modified in the centre by a modest contraction due to the presence of stars (Duffy et al. 2010; Di Cintio et al. 2014; Schaller et al. 2015).

Baryon contraction is less important in haloes of mass $M_{200} \sim 10^{14}$ M$_\odot$ which are well fit by an NFW profile, as can be seen in Fig. 2, where the solid magenta line shows the best-fitting NFW profile. The fit was performed using all radial bins from the resolution limit, $r_c \sim 3$ kpc, to the virial radius, $R_{vir} \sim 2$Mpc. We have checked that the best-fitting parameter values are largely insensitive to the exact radial range used, provided that both the $\rho(r) \to r^{-1}$ and $\rho(r) \to r^{-3}$ regimes of the profile are well sampled. In all but one case, the magenta line closely tracks the DM profile plotted as black squares. The exception is halo 5 (bottom row, middle panel) which shows a slight deviation from the NFW form in the radial range $3-7$ kpc, where some contraction is seen, possibly as a result of the recent accretion of a large substructure. The best-fitting NFW parameters are listed in Table 2. The mean and scatter in concentration (nearly a factor of 2) of our haloes are consistent with the results obtained for relaxed haloes in the Millennium simulation by Neto et al. (2007), who found a concentration, $c_{200} = 4.51^{+0.71}_{-0.62}$, for haloes of mass $M_{200} = 10^{14}$ M$_\odot$.

While the DM is well described by an NFW profile, the *total matter* profile in our haloes is not. In our study of the entire halo population in the EAGLE simulation, we introduced the following fitting formula for the total matter (Schaller et al. 2015):

$$\frac{\rho(r)}{\rho_{cr}} = \frac{\delta_c'}{\left(r/r_s'\right)\left(1 + r/r_s'\right)^2} + \frac{\delta_i}{\left(r/r_i\right)\left(1 + (r/r_i)^2\right)}. \quad (2)$$

The first term has the NFW form and describes the overall shape of the profile; the second term is a correction that reproduces the stellar cusps ($\rho_* \propto r^{-3}$), together with any DM contraction due to the presence of baryons. The dark yellow solid lines in the six panels of Fig. 2 show the best-fitting profiles of this kind to each halo which, as may be seen from the figure, represent the data well over the entire resolved radial range. The best-fitting parameter values are listed in Table 3.

4 THE INNER DENSITY PROFILE

A testable prediction from simulations evolving only DM of the ΛCDM model is that the average slope of the inner mass profile ($r \ll r_s$) should tend to the NFW value of -1. Steeper profiles might be explained by baryon effects causing some contraction. Significantly shallower profiles in massive haloes, on the other hand, would be more difficult to explain. Explosive baryon effects could lower the inner DM density, and even induce cores, but only in dwarf galaxies (Navarro et al. 1996a; Read & Gilmore 2005; Pontzen & Governato 2014). In massive haloes, Martizzi et al. (2012) have argued that AGN feedback could introduce small ($\sim$10 kpc) cores, but it is unclear if this kind of feedback is compatible with the observed stellar masses of BCGs and the baryon fractions of clusters. Shallower inner profiles could also be generated if the DM is self-interacting (Vogelsberger et al. 2012; Rocha et al. 2013).

4.1 Total mass profiles: simulation results

A quantity that can be derived from observational data in selected samples of rich clusters is the *average logarithmic slope* of the inner density profile of the total mass, that is DM and baryons (e.g. Sand et al. 2004; Newman et al. 2013a):

$$\gamma_{tot} \equiv - \left\langle \frac{d \log \rho_{tot}(r)}{d \log r} \right\rangle_{r \in [0.003 R_{200}, 0.03 R_{200}]}, \quad (3)$$

where the average is over the radial range $[0.003 R_{200}, 0.03 R_{200}]$. It is important to recognize that the radial range typically probed by the data is *not* the asymptotic regime, $r \to 0$, where the NFW profile tends to $\rho(r) \propto r^{-1}$. Instead, in the region probed by observations, the NFW formula (equation 1) predicts values of the inner slope significantly steeper than -1 (i.e. $\gamma_{tot} > 1$):

$$\gamma_{tot} = 1 + \log_{10} \left(\frac{(1 + 0.03 c_{200})^2}{(1 + 0.003 c_{200})^2} \right), \quad (4)$$

which, for the expected range of cluster concentrations ($c_{200} \in [3, 5]$), gives $\gamma_{tot} \approx 1.1$.

The radial range over which γ_{tot} is typically measured in observational studies is shown for our clusters as a grey shaded region in each panel of Fig. 2. The values of the slope predicted by our simulations in this range are shown above the data points. Values of γ_{tot} for our halo sample are plotted as a function of halo mass in Fig. 3 (large green diamonds), which also includes data for haloes in the simulation volume that are less massive than those in our main sample (small green diamonds). The black dashed line shows the slope of the NFW profile obtained from equation (4) and the mass–concentration relation of Schaller et al. (2015). As a guide, we include two dash–dotted lines showing where profiles may be
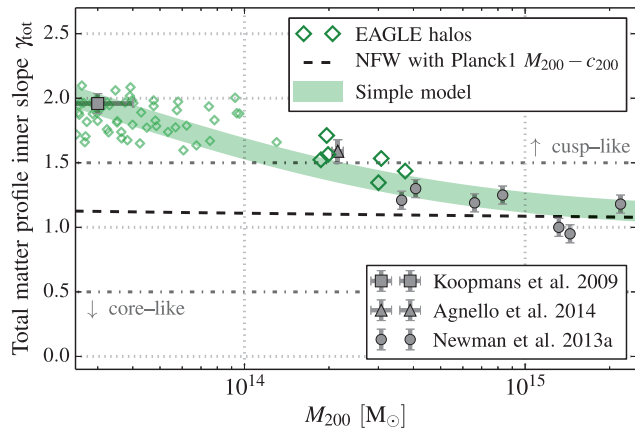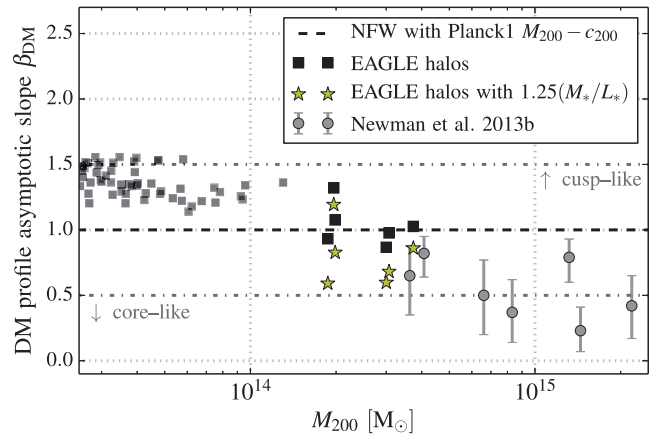
Figure 3. The logarithmic slope of the inner density profile of the total mass distribution, $\gamma_{\rm tot}$, as a function of halo mass, M_{200}. The dashed line shows the average slope of the NFW profile over the range in which $\gamma_{\rm tot}$ is defined. The large green diamonds represent the six EAGLE haloes in our sample and the small green diamonds the smaller mass EAGLE haloes. The grey symbols with error bars are the slopes measured by Koopmans et al. (2009) for 58 early-type galaxies in the SLACS survey (square), the slope inferred by Agnello et al. (2014) from globular clusters orbits in M87 (triangle) and the slopes measured by Newman et al. (2013a) for seven massive clusters (circles). As a guide, the grey dash–dotted lines demarcate slopes that may be construed as 'core-like' and 'cuspy'. The lower mass EAGLE clusters are cuspier than an NFW halo because of the contribution of the stellar component which, however, becomes increasingly less important for larger mass haloes. The Newman et al. (2013a) data lie along the extrapolation of the trend seen in the EAGLE clusters.

Figure 4. The asymptotic logarithmic slope of the inner DM density profile, $\beta_{\rm DM}$, as a function of halo mass, M_{200}. The dashed line shows the NFW value of -1. The large black squares show the values measured for the six massive clusters in our EAGLE sample and the small black squares those measured for smaller EAGLE clusters. The yellow stars show the slopes that would be inferred for our sample if the stellar mass-to-light ratio is overestimated by 25 per cent (see Section 5.3 for details). The grey circles with error bars are the values inferred by Newman et al. (2013b). As in Fig. 3, the grey dash–dotted lines demarcate slopes that may be construed as 'core-like' and 'cuspy'.

considered to be 'cuspy' ($\gamma_{\rm tot} > 1.5$) or 'core-like' ($\gamma_{\rm tot} < 0.5$). The exact position of these lines is, of course, arbitrary.

The high-mass tail of the cluster population is not represented in the limited volume of the EAGLE simulation. However, the general behaviour of massive clusters can be readily inferred from the trends seen for smaller haloes. A halo of mass $M_{200} \approx 2 \times 10^{15}\,\rm M_\odot$ has $R_{200} \approx 2\,\rm Mpc$ and thus $\gamma_{\rm tot}$ is centred (logarithmically) around $r = 20\,\rm kpc$. In this region the profile is dominated by DM, even in the case of large, extended galaxies. Thus, $\gamma_{\rm tot}$ is unaffected by the BCG and directly reflects the slope of the DM profile which Schaller et al. (2015) showed has a slope close to or slightly steeper than the NFW value, as given by equation 4. Thus, for haloes of $M_{200} \approx 2 \times 10^{15}\,\rm M_\odot$ we expect $\gamma_{\rm tot} \approx 1.1$. This conclusion is consistent with the collisionless model of Laporte & White (2014) who also find slopes close to the NFW value for $M_{200} \sim 10^{15}\,\rm M_\odot$ clusters.

Based on this argument we can construct a simple model, consistent with the results for low-mass haloes, to extrapolate the slopes measured for the EAGLE clusters into the mass range appropriate to rich clusters. This model is designed to capture the general behaviour of $\gamma_{\rm tot}$ on mass scales larger than $M_{200} \approx 2 \times 10^{13}\,\rm M_\odot$. It assumes that the total matter profile is made up of an NFW DM halo plus a stellar component which, in order to be consistent with relevant observational analyses, we take to be a 'dual pseudo isothermal elliptical mass distribution' (dPIE; Elíasdóttir et al. 2007). The value of the halo mass determines the concentration of the halo and we infer the stellar mass of the central galaxy from abundance matching (e.g. Moster et al. 2013). For the dPIE profile, we adopt the mean scale radius and core radius of the best-fitting profiles for our BCGs and keep them fixed while varying the normalization to match the stellar mass of interest. (We verified that varying the values of the parameters of this model does not affect our results.) In this way

we construct the total mass profile and measure its slope, which we show as the green band in Fig. 3. The slopes of the total mass profiles of the largest EAGLE clusters plotted in Fig. 2 are slightly steeper than the NFW value over the radial range over which $\gamma_{\rm tot}$ is defined. This mostly reflects the contribution of stars to the inner matter density. By contrast, the values inferred for more massive clusters are closer to the NFW value.

We now turn to the slope of the DM profiles. Unlike the total mass profile, the DM profile cannot be measured directly from observations, but must instead be inferred through detailed modelling, which requires a number of assumptions. The DM profile in the simulations can, of course, be directly measured and the simulations can be used to test the consistency of the assumptions required in the modelling of the observational data.

The average slope of the DM density profile over the same radial range used to define $\gamma_{\rm tot}$ ([$0.003R_{200}, 0.03R_{200}$]) for our sample of simulated clusters is indicated by the black line in the grey shaded regions in Fig. 2. Some observational analyses attempt to constrain the asymptotic slope, $\beta_{\rm DM}$, of a generalized NFW profile (gNFW):

$$\frac{\rho_{\rm gNFW}(r)}{\rho_{\rm cr}} = \frac{\delta_{\rm c}}{(r/r_{\rm s})^{\beta_{\rm DM}}(1 + r/r_{\rm s})^{3-\beta_{\rm DM}}}. \tag{5}$$

This profile is often used to quantify deviations from the NFW form to which it reduces for $\beta_{\rm DM} = 1$ (equation 1). We fit this profile to the DM of our simulated haloes and plot the resulting values of $\beta_{\rm DM}$ as a function of halo mass, M_{200}, in Fig. 4, which is the DM analogue of Fig. 3. As may be seen, the EAGLE clusters (black squares) have inner slopes consistent with the NFW expectation (equation 4). As was the case for the total matter profile, the inner DM profile slopes also show significant scatter, with $\beta_{\rm DM}$ varying by as much as ~ 0.4 for haloes of similar mass.

4.2 Total mass profiles: overview of recent observational data

By combining different observational techniques, the *total* matter profile of clusters can be estimated. Two techniques have been used

to probe the central mass distributions: strong lensing and modelling of the orbits of globular clusters (GC) or BCG stars. The former relies on a chance alignment of the cluster with a background galaxy and is, by nature, rare since only a few galaxy clusters present strong lensing arcs at the radii of interest. Similarly, the use of GC orbits as tracers of the potential is limited to clusters that are close enough for the GCs to be unambiguously detected. Stellar velocity dispersion measurements of the central galaxy can also be used to constrain the mass near the centre of the halo but high-resolution spectroscopy is required. We will now compare our simulated cluster slopes to recent observational data. Although there is a wealth of data available for profiles at large radii, we focus exclusively on the inner regions which are the most sensitive to the nature of the DM.

The grey square with error bars at the low mass end of Fig. 3 shows the average slope measured for 58 early-type galaxies in the SLACS survey by Koopmans et al. (2009) using a combination of strong lensing and stellar velocity dispersion measurements. Our simulation agrees perfectly with this data point. At the more massive end, Newman et al. (2013a) derived total mass profiles, $\rho_{\text{tot}}(r)$, from projected mass profiles, which they estimated using strong and weak lensing data, together with the surface brightness and resolved stellar kinematics of the BCGs in a sample of seven clusters. The grey circles with error bars in Fig. 3 show their results. Five of these clusters have higher masses than the largest clusters in the relatively small EAGLE simulation volume, but the two lightest ones fall in the region represented in our simulation. Their values of γ_{tot} agree very well with those measured directly in our simulated clusters while the values for the more massive five lie in the region predicted by the simple model used to extrapolate the EAGLE results described in Section 4.1.

An independent measurement of the total inner density profile which does not rely on lensing data was carried out by Agnello et al. (2014) using the orbits of GCs in the halo of M87. The slope, γ_{tot}, inferred from their best-fitting broken power-law model is shown as a triangle with error bar In Fig. 3, this data point also agrees extremely well with the results for the EAGLE clusters.

We conclude that the inner density profiles of the *total* mass distribution in the EAGLE clusters are in good agreement with the best current data Koopmans et al. (2009), Newman et al. (2013a) and Agnello et al. (2014). In both simulated and observed clusters, the inner profile slopes exhibit considerable scatter reflecting the variety of factors that affect the density structure, such as halo assembly history, shape and substructure distribution, BCG star formation and merger history, etc.

4.3 DM density profiles

The situation is more complicated for the density profile of the DM since this is not directly accessible to observations. Instead, this profile must be inferred from a model to disentangle the contributions of the dark and visible components from the measured total mass profile. Wide radial coverage is needed fully to sample the two components and effect the decomposition. Strong lensing data seldom sample the range, $r \lesssim 10 \, \text{kpc}$, where the influence of baryons starts to play a role and so lensing data need to be supplemented by, for example, kinematical data for the stars of the BCG. Such data exist for only a handful of clusters (e.g. Sand et al. 2004; Newman et al. 2013a). The study by Newman et al. (2013a) is particularly interesting by virtue of the quality of the data and the comprehensive analysis performed. In the remainder of this paper, we will therefore focus on the comparison with these data.

The model assumed by Newman et al. (2013a) is a gNFW profile for the DM and a dPIE profile for the galaxy. The authors estimated the parameters values that minimize the difference between the model and the inferred lensing mass, the measured profiles of stellar velocity dispersion, $\sigma_{\text{l.o.s.}}$, and surface brightness, *S*. In addition to the parameters describing the DM profile, the minimization procedure also constrains the stellar mass-to-light ratio, Υ_*. This is an important parameter since, at a given radius, it is degenerate with the dark matter mass: one can always trade DM for unseen stellar mass at that radius,

$$\rho_{\text{DM}}(r) = \rho_{\text{tot}}(r) - \Upsilon_* \times S(r). \tag{6}$$

This degeneracy can be broken by measuring the total density and surface brightness as a function of projected radius, *R*, and assuming that the stellar mass-to-light ratio is constant.

The values of β_{DM} (equation 5) inferred by Newman et al. (2013b) for their sample of clusters are shown as grey circles in Fig. 4. The error bars indicate the 16th and 84th percentiles of the posterior distribution of β_{DM} returned by their model (not including systematics). These lie well below the values for the EAGLE clusters (black squares) and are clearly inconsistent with them given the quoted errors. From our earlier discussion it seems unlikely that the discrepancy can be due to the slightly smaller masses of the EAGLE clusters compared to those in the observed sample, since the EAGLE clusters have DM inner slopes that are either close to or slightly steeper (due to contraction) than the NFW value. Thus, we conclude that profile slopes as shallow as those inferred by Newman et al. (2013b) are not present in ΛCDM simulations with the baryon physics modelled in EAGLE. This conclusion is surprising since the *total* mass profiles of the real and simulated clusters agree remarkably well. We will now discuss possible reasons for this apparent discrepancy.

5 DISCUSSION

We saw in the preceding section that the inner slopes of the density profiles of the DM haloes in the EAGLE clusters differ from the profiles inferred by Newman et al. (2013b) for their sample of seven clusters. There are several possible explanations for the discrepancy. One is that the simulations do not model the correct physics. This would be the case if the DM does not consist of cold collisionless particles but of particles that undergo self-interactions (e.g. Spergel & Steinhardt 2000; Vogelsberger et al. 2012; Rocha et al. 2013). Cluster simulations would be required to determine whether the slopes found by Newman et al. (2013a) can be explained for reasonable values of the self-interaction cross-section and a reasonable model for the baryonic physics.

Another possibility is that the DM is indeed cold and collisionless but the injection of energy from an AGN has flattened the NFW cusp. This is a scaled-up version of the mechanism originally invoked by Navarro et al. (1996a) to explain the possible existence of cores in dwarf galaxies. The simulations of Martizzi et al. (2012) show precisely this effect, but kiloparsec-scale cores are only produced by injecting very large amounts of AGN energy into the surrounding gas. Our simulations have weaker AGN feedback, as required to achieve a good match to the massive end of the observed stellar mass function, and do not produce cores. It is unclear if feedback as intense as that required by Martizzi et al. (2012) would lead to a similarly good match to the global properties of the galaxy population (Crain et al. 2015; Furlong et al. 2015; Schaye et al. 2015).

The disagreement between the inner DM profiles of the EAGLE clusters and of the clusters in the Newman et al. (2013b) sample could also be due to a mismatch between the directly observable quantities, $\sigma_{l.o.s.}(R)$ and $S(R)$, and the corresponding quantities for the EAGLE clusters, or to systematic effects either in the selection of the observational sample or in the method used to inferred the inner DM slopes. We will now discuss these possibilities.

The most direct way to carry out the comparison would be to replicate the analysis of Newman et al. (2013a) on our simulated clusters. Unfortunately, the exact model and fitting pipeline used by them is not available to us and, as we will see below, the results are very sensitive to small changes in the assumption of the analysis pipeline. We therefore restrict our comparison to directly observable quantities and discuss how some of the assumptions made could impact the inferred values of β_{DM}.

5.1 Surface brightness profiles

Stars are the dominant contributors to the density in the central regions of the EAGLE clusters and probably also in the real data. Clearly, if the surface brightness of the simulated clusters differed significantly from the observations, subtraction of this component could lead to different results for the slope of the DM profile in the two cases.

As discussed in Section 2.2, the luminosity of each stellar particle in the simulations is obtained from a BC03 population synthesis model assuming the Chabrier (2003) IMF. To compare our haloes with observations, we derive magnitudes in the four *HST* filters ($F606W$, $F625W$, $F702W$ and $F850LP$) used by Newman et al. (2013a). We placed our clusters at $z = 0.25$, the mean redshift of that sample, by redshifting the spectra before applying the *HST* filters[2] and dimming the luminosities by a factor $(1 + z)^{-4}$. To account for the somewhat smaller masses of the EAGLE clusters compared to those in the sample of Newman et al. (2013a) (whose mean mass is $M_{200} = 1.03 \times 10^{15}\,M_\odot$) we scaled up their surface brightnesses by a modest factor, $(M_{200}/1.03 \times 10^{15}\,M_\odot)^{1/6}$, derived assuming that the luminosity $L \propto M_{200}^{1/2}$ and that the stellar density remains constant in the narrow range or relevant halo masses.[3] We then chose 10 000 random lines of sight through each cluster and projected the particles along those axes on to the plane of the (virtual) sky. Finally, we binned the particles radially from the centre of the potential to derive the stellar surface brightness.

The surface brightness profiles of our six EAGLE clusters are plotted in Fig. 5. The solid lines show the mean profiles averaged over 10 000 lines of sight in the four different *HST* filters and the shaded regions the 1σ scatter around these values. The black symbols correspond to the measurements taken from Newman et al. (2013a) with physical radii derived from their angular sizes and redshift measurements. Although the EAGLE clusters have a slightly smaller total mass, the surface brightness of their central galaxies are in quite good agreement with those of the Newman et al. (2013a) sample: the shapes of the profiles are somewhat different, with our clusters having a slightly shallower inner slope than the observed clusters.

A striking feature of Fig. 5 is the small scatter in the simulations for the different lines of sight. Near the centre the scatter is dominated by the presence of foreground satellites rather than by the orientation of the BCG. Another interesting feature is the large

object-to-object variation, both in the simulations, where the central luminosities vary by around 0.8 mag, and in the observations, where the variation is even larger, almost 2 mag, with no apparent correlation with halo mass. Our simulated haloes lie well within the observational scatter but themselves show somewhat smaller scatter. At large radii, five out of our six clusters appear to be slightly more luminous than the real clusters. However, this is the region where the observational data terminate and where background subtraction becomes significant.

We conclude that the surface brightness profiles of the EAGLE clusters are sufficiently similar to those of the Newman et al. (2013b) sample that differences in the starlight distribution cannot be the reason for the discrepancy between the DM profiles in the simulations and those inferred from the data.

5.2 Velocity dispersion profiles

The line-of-sight stellar velocity dispersion, $\sigma_{l.o.s.}$, of our six haloes as a function of projected radius is shown in Fig. 6. Since the EAGLE clusters are less massive than the clusters in the sample of Newman et al. (2013a), in order to facilitate a comparison, the velocity dispersions of the simulated clusters have been rescaled, as before, to the mean mass of the Newman et al. (2013a) sample by multiplying the velocity dispersions by the corresponding factor $(M_{200}/1.03 \times 10^{15}\,M_\odot)^{1/6}$.

The measured $\sigma_{l.o.s.}$ is quite sensitive to the shape of the galaxy and the viewing angle. The axial ratios, of the six EAGLE BCGs (computed from the principal axes of the inertia tensor of the star particles $a > b > c$) are illustrated in Fig. 7 where the projection along the minor axis is shown at the top of each panel and the projection along the major axis at the bottom. Four of the six EAGLE clusters (1, 2, 5 and 6) are clearly prolate and the remaining two are close to spherical. We viewed the BCGs from 10 000 random directions placing an imaginary slit at a random angle on the plane of the sky centred on the halo potential minimum and measured the velocity dispersion of the stars as a function of projected radius, subtracting any bulk rotation.

As expected, the line-of-sight velocity dispersions increase with radius. In the inner regions ($r \lesssim 10$ kpc) gravity is dominated by the stars. The 1σ scatter from the different viewing angles, shown as a grey shaded region in Fig. 6, is rather large at all radii for all objects, of the order of 10 per cent or more for all but two of the haloes. The black solid line shows $\sigma_{l.o.s.}$ for a line of sight chosen along the major axis of each BCG. In three of our six clusters (haloes 2, 5 and 6), the velocity dispersion along this particular line of sight is biased high and, in two cases, it falls outside the 1σ scatter. As can be seen on Fig. 7, these are the three most prolate haloes in our sample. A bias in the line-of-sight velocity dispersion is expected since orbits in prolate haloes have larger velocities along the direction of elongation. These objects would nevertheless appear spherical on the sky when viewed in this direction since the axis ratios b/c are close to unity. The three most spherical haloes do not exhibit any particular bias when viewed along their major axis, as expected.

The line-of-sight velocity dispersion profiles of the seven clusters studied by Newman et al. (2013a) are shown as dashed colour lines with error bars in each panel of Fig. 6. The six rescaled EAGLE clusters have dispersions that fall within the scatter of the observational data. Thus, unless there is a strong orientation bias for the BCGs in the cluster sample of Newman et al. (2013a), a mismatch in velocity dispersion profile cannot be the cause of the difference between the slopes of the DM haloes in the EAGLE clusters and those inferred by Newman et al. (2013a).

---

[2] Effectively applying a reverse *K*-correction.

[3] Note that this is a more conservative rescaling factor than simply assuming $L \propto M_{200}$.
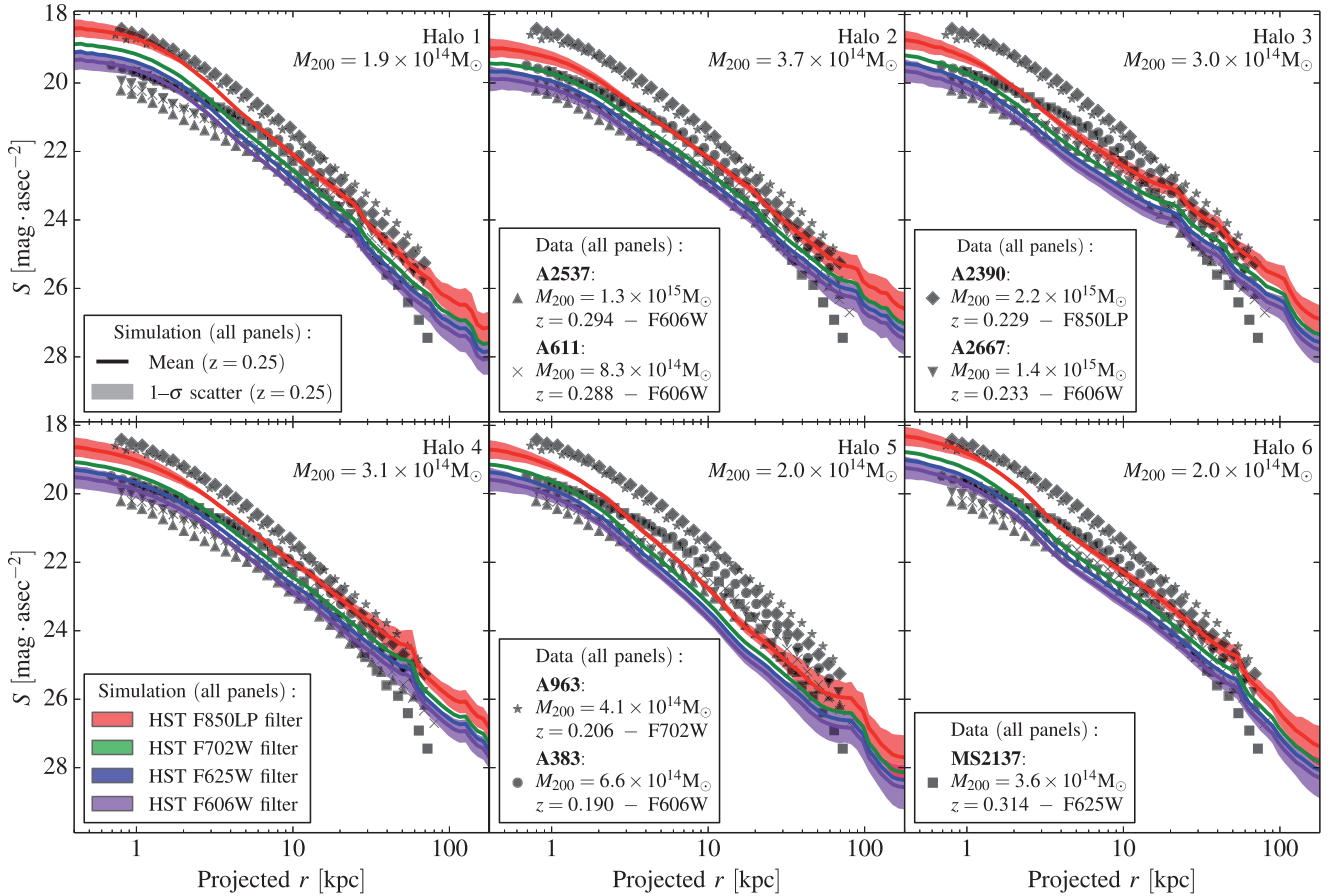
Figure 5. Surface brightness profiles of the six EAGLE clusters in our sample (placed at $z = 0.25$) in the four *HST* filters (from top to bottom: *F850LP*, *F702W*, *F625W* and *F606W*) used by Newman et al. (2013a) in AB magnitudes per arcsec^{-2}. The solid lines show the mean profile scaled by the factor, $(M_{200}/1.03 \times 10^{15} \, M_\odot)^{1/6}$, averaged over 10 000 random lines of sight. The shaded regions show the 1σ scatter for the reddest and bluest filters. (The other filters have similar scatter.) The black symbols show the measured surface brightness profiles of the seven clusters observed by Newman et al. (2013a) whose redshifts are given in the legend together with the filter used. The clusters in the simulations have surface brightness profiles in reasonable agreement with those observed.

Since the projected mass density of a prolate halo is also largest along its major axis, there is a potential and well-understood selection bias in samples of clusters selected for lensing studies. If the BCGs in the sample of Newman et al. (2013a) were prolate and preferentially viewed along their major axes, then, as shown in Fig. 6, the observed line-of-sight velocity dispersions would be biased high. This would lead to an overestimate of the mass enclosed within the radius sampled by the velocity dispersion data. In the absence of other information, it would not be possible to separate the relative contributions to this estimate from stars and DM. However, the available lensing data constrains the total mass (and, in the case of radial arcs, also the slope of the profile) in the central regions of the cluster. This, together with the inferred stellar profile, restricts the fits to the combined data and this could lead to an underestimate of the DM mass near the centre of the clusters.

Such an effect could explain the difference between the slopes of the DM profiles inferred by Newman et al. (2013a) and those measured for the EAGLE clusters. However, Newman et al. (2013a) argue that their sample does not suffer from such a bias since the distribution of ellipticities in it is consistent with that of the BCG population as a whole. In the case of A383, for which the X-ray data indicate is elongated along the line of sight, they explicitly use a non-spherical model.

5.3 Mass-to-light ratio

As mentioned in Section 4.2, the stellar mass density at a given radius is degenerate with the DM mass density at that radius (equation 6). In the simulations we know the stellar mass and so we can subtract it exactly from the total mass. The resulting value of the inner DM halo slope was shown in Fig. 4. By contrast, in the observational sample the stellar mass must be derived from an estimate of the stellar mass-to-light ratio, Υ_*.

Newman et al. (2013a,b) treated Υ_* as a parameter in their model over which they marginalize. The value of Υ_* is determined by the unknown IMF; In their Bayesian model, they adopt a prior distribution that effectively restricts the IMF to be between 1.5 times lighter than Chabrier and 2 times heavier than Salpeter. Despite this wide range, the posterior distribution of Υ_* is limited by the shape of the assumed prior in three out of the seven BCGs, suggesting that the mass-to-light ratio is not well constrained by the data. Had we in our simulations (which adopt a Chabrier IMF) subtracted a stellar mass inferred by incorrectly assuming a Salpeter IMF, we would have overestimated Υ_* by 65 per cent. This would have led us to infer a negative slope for the inner DM density profile in three out of our six clusters, implying virtually no DM at their centres!
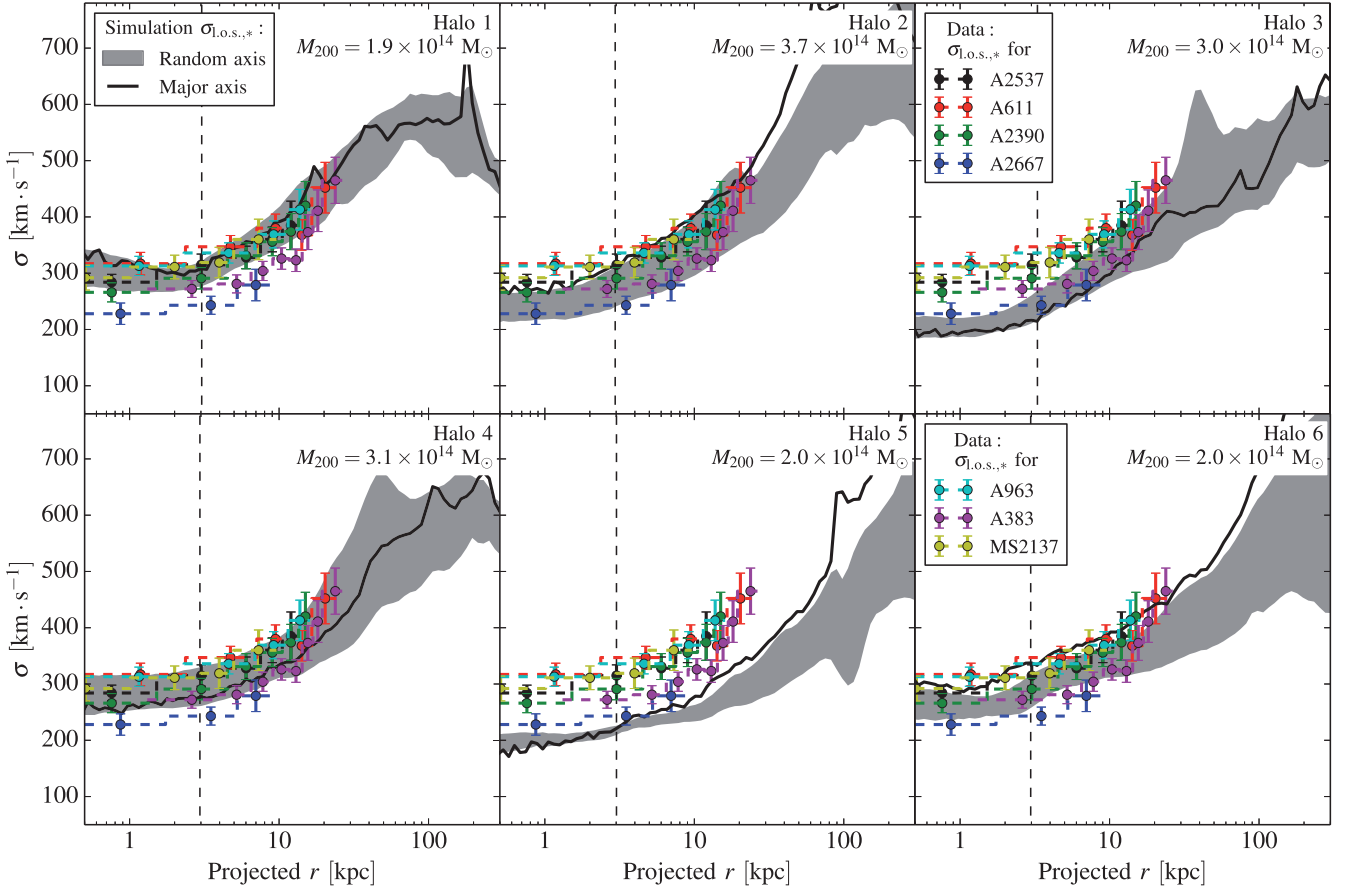
Figure 6. Stellar velocity dispersion along the line of sight as a function of projected radius for the six EAGLE clusters listed in Table 1. The dispersions have been rescaled by a factor $(M_{200}/1.03 \times 10^{15}\,\mathrm{M_\odot})^{1/6}$ to correct for the slightly lower masses of these clusters compared to the mean of the observational sample of Newman et al. (2013a). The grey shaded region is the 1σ scatter obtained when looking at the haloes from 10 000 random lines of sight. The black solid line is the profile as seen from a line of sight oriented along the galaxy's major axis. The vertical dashed line on each panel shows the 3D convergence radius, r_c. The coloured dashed lines with error bars are the measurements for the seven clusters observed by Newman et al. (2013a). In three of the six EAGLE haloes the velocity dispersion profile measured along the major axis is biased high.

In Fig. 4, we show the effect of overestimating Υ_* by a much smaller factor of only 25 per cent. The inferred slopes, shown by yellow stars, are significantly shallower than the true slopes and have more scatter. Such a relatively small systematic error would be sufficient to bring the inferred slopes in the simulations into agreement with the estimates of Newman et al. (2013b).

The estimate of Υ_* in the model of Newman et al. (2013b) requires the measurement of the line-of-sight velocity dispersion profile, $\sigma_{\mathrm{l.o.s.}}$, of the BCG, as a function of projected separation, R. In dynamical equilibrium, $\sigma_{\mathrm{l.o.s.}}$ is given by the Jeans equation (e.g. Binney & Tremaine 1987; Cappellari 2008):

$$\sigma^2_{\mathrm{l.o.s.}}(R) = \frac{2G}{\Sigma_*(R)} \int_R^\infty \frac{\mathcal{F}(r, R, \beta)\rho_*(r)M_{\mathrm{tot}}(r)}{r^{2-2\beta}}\,\mathrm{d}r, \qquad (7)$$

where $\rho_*(r)$ is the 3D density of tracers (the stars) whose surface density is $\Sigma_*(R)$; $M_{\mathrm{tot}}(r)$ is the total enclosed mass; $\beta = 1 - \sigma^2_\theta/\sigma^2_r$ is the velocity anisotropy parameter, here assumed to be independent of radius, with σ_r and σ_θ the radial and tangential velocity

dispersions, respectively,[4] and

$$\mathcal{F}(r, R, \beta) = \frac{R^{1-2\beta}}{2}\left[\beta B\left(\frac{R^2}{r^2}; \beta + \frac{1}{2}, \frac{1}{2}\right)\right.$$
$$\left. - B\left(\frac{R^2}{r^2}; \beta - \frac{1}{2}, \frac{1}{2}\right) + \frac{\sqrt{\pi}(3 - 2\beta)\,\Gamma(\beta - \frac{1}{2})}{2\Gamma(\beta)}\right],$$

where $\Gamma(x)$ is the Gamma function and $B(z; a, b)$ is the incomplete Beta function. In the limit where $\beta \to 0$, $\mathcal{F}(r, R, \beta)$ reduces to

$$\lim_{\beta \to 0} \mathcal{F}(r, R, \beta) = \sqrt{r^2 - R^2}.$$

In the more general case where β is a function of r, the problem of reconstructing the mass distribution becomes more complex. Solutions for specific forms of $\beta(r)$ have been derived by Mamon & Boué (2010).

In the Jeans equation, the velocity anisotropy parameter and the mass are degenerate. In their analysis Newman et al. (2013a) assumed $\beta = 0$ i.e. isotropic orbits. This assumption is a source of a potentially significant systematic error which Newman et al.

---

[4] With this definition, $\beta = 0$, 1 and $-\infty$ correspond to isotropic, radially biased and circularly biased orbits, respectively.
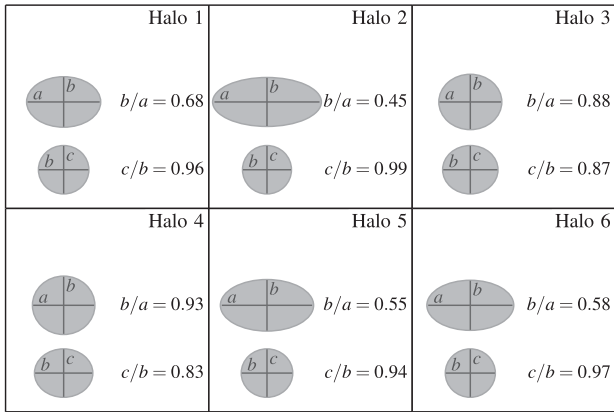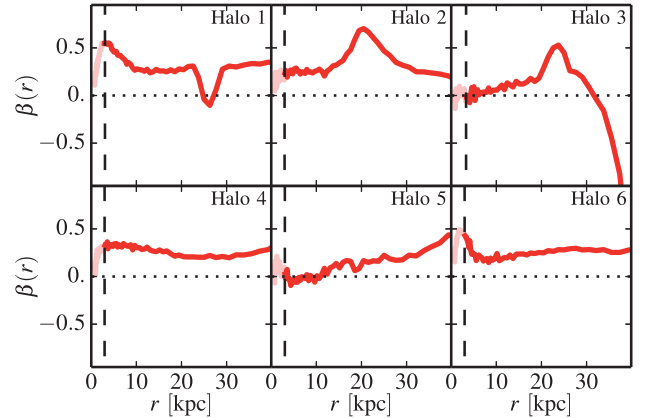
Figure 7. The projection of the central stellar component of the six EAGLE clusters along the minor axis (top ellipse in each panel) and major axis (bottom ellipse). The axes ratios are given next to each ellipse. Four of the galaxies are clearly prolate and the remaining two are slightly oblate. Prolate galaxies have velocity dispersions that are biased high (Fig. 6) when observed along their major axis.

Figure 8. Stellar anisotropy profile $\beta(r)$ as a function radius for the six EAGLE clusters over the radial range relevant to the stellar kinematics analysis. The vertical dashed line on each panel shows the 3D convergence radius, r_c and the profiles at lower radii are shown using shaded lines. Two BCGs are consistent with $\beta = 0$ but would be better fit with a non-constant β. Ignoring complex features, the other four clusters present more radially biased orbits with $\beta(r) \approx 0.25$. A single profile shape for $\beta(r)$ cannot be used to characterize all six of our BCGs.

(2013a) investigated. They found that if the orbits were mildly radially biased with a constant value of $\beta = +0.2$, then Υ_* would be overestimated by 30 per cent. In our simulations we can calculate β directly for the stars in the model BCGs. The variation of β with radius is shown in Fig. 8. We find that, in general, β varies with radius over the range where Newman et al. (2013a) obtained kinematical data. In two of our clusters, β is close to zero over this range, but in the other four, β becomes increasingly positive with radius, with a mean value of ∼0.2–0.3. Complex features, which cannot be described by a simple linear form for $\beta(r)$ are also present, precluding the reconstruction of $M(r)$ from an assumed functional form for $\beta(r)$. It is also worth mentioning that the profile of $\beta(r)$ is uncorrelated with the shape of the BCGs: of the two cases with nearly isotropic orbits (haloes 3 and 5), one is nearly spherical and the other very elongated (see Fig. 7).

In order to test the assumption of anisotropy, we inverted equation (7) numerically. Extracting $\sigma_{l.o.s.}(R)$, $\Sigma_*(R)$ and $\rho_*(r)$ from the simulated clusters we reconstructed $M_{tot}(r)$ assuming $\beta = 0$ and compared the result to the actual value. We found that for this assumption the reconstruction overestimates the value of M_{tot} by factors ranging from 10 to over 100 per cent. Repeating this analysis, this time assuming $\beta = 0.2$, led to errors of comparable size for the four haloes that display an anisotropy profile differing significantly from $\beta(r) = 0.2$ (see Fig. 8). Thus, for most of our clusters, the analysis of Newman et al. (2013a) would have overestimated the stellar mass-to-light ratio by more than the 25 per cent which, according to Fig. 4, would reconcile their results with our simulations. This test, however, does not take into account constraints on the *total* mass profile from lensing data at large radii, which could exaggerate the dependence of the inferred value of M_{tot} near the centre on the assumed value of β.

In real clusters, additional uncertainties are introduced by factors such as an assumed form for the 3D stellar mass density profile, $\rho_*(r)$, and an assumption for the value of the stellar mass-to-light ratio, Υ_*. This is mitigated by constraints on M_{tot} provided by lensing data although, in general, the lensing and kinematical data do not overlap sufficiently to separate the contributions from the stellar mass and the dark mass. In the model of Newman et al. (2013a), Υ_* is coupled to other parameters such as the slope of the total mass profile, so that the effect on the quantity of interest, β_{DM}, is

difficult to anticipate without re-running their pipeline for different assumptions for the velocity anisotropy. For example, Newman et al. (2013b) tried a solution for the case of constant anisotropy, $\beta = 0.2$, and found an increase in β_{DM} of about 0.13, which would bring their data closer to our simulations. What we can say with certainty is that the kinematical model assumed by Newman et al. (2013a) is not consistent with the EAGLE BCGs, offering a possible explanation for the discrepancy in the DM density slopes.

Constraining the anisotropy, β, in cases in which, as in our simulated clusters, it varies with radius is not straightforward. Yet, this is what is required in order to lift the degeneracy between anisotropy and mass which lies behind the degeneracy between Υ_* and the DM profile slope. The use of Integral Field Spectroscopy may help constrain this quantity in future studies.

6 SUMMARY AND CONCLUSIONS

We have studied the density profiles of the six most massive clusters in the largest EAGLE simulation (Schaye et al. 2015). The EAGLE simulation was calibrated to provide a good match to the observed stellar mass function and galaxy sizes in the local universe, suggesting that it gives a realistic representation of the local galaxy population. Due to the relatively small volume of the simulation (100^3 Mpc^3), the clusters selected for this study tend to be somewhat less massive (mean $M_{200} = 2.6 \times 10^{14}$ M$_\odot$) than the seven clusters studied by Newman et al. (2013a) (mean $M_{200} = 1 \times 10^{15}$ M$_\odot$) to which we compare our results in particular detail, although the two lightest clusters in the observational sample have similar masses to the three most massive EAGLE clusters. For these clusters Newman et al. (2013a) have obtained strong and weak lensing as well as stellar kinematical data for the BCGs.

The total mass density profile of the EAGLE clusters is dominated in the central parts ($r < 10$ kpc) by the BCG. The presence of the central galaxy makes the total mass profile steeper than an NFW profile near the centre. The inner slope of the total mass profile (defined as the average slope in the range $r = 4 - 35$ kpc) agrees remarkably well with the slopes measured by Newman et al. (2013a) for their clusters, with the corresponding slopes measured by Koopmans et al. (2009) for 58 early-type galaxies in the SLACS

survey, and with the slope inferred by Agnello et al. (2014) from the kinematics of GCs around M87.

The DM density profile of the EAGLE clusters is very well described by the NFW profile over the entire resolved radial range, $r = 3$-2000 kpc. By contrast, Newman et al. (2013b), after subtracting the contribution of the stars, inferred significantly shallower DM slopes for their clusters in the inner regions, in contradiction with our own results. This discrepancy is puzzling because, in addition to the total mass density profiles, the surface brightness and line-of-sight velocity dispersion profiles of the EAGLE clusters agree quite well with those of the Newman et al. (2013a) clusters.

We have considered possible explanations for the discrepancy between the inner DM density profiles of the EAGLE clusters and those inferred by Newman et al. (2013b). A possible interpretation is that the simulations lack the correct physics, either because the DM is not collisionless (e.g. Spergel & Steinhardt 2000; Vogelsberger et al. 2012; Rocha et al. 2013) or because extreme baryon processes not represented in our simulations have destroyed the inner DM cusps (Martizzi et al. 2012). Baryon effects associated with AGN in the EAGLE simulations are not strong enough to produce density cores; yet the simulation reproduces the exponential cut-off in the stellar mass function remarkably well.

An alternative explanation for the discrepancy is that the uncertainties in the determination of the inner DM density slope were underestimated by Newman et al. (2013b). In particular, their analysis relies on an accurate estimate of the stellar mass-to-light ratios of the BCGs. We showed that a systematic overestimation of this ratio by only 25 per cent would reconcile the observational data with our results. An effect of this size could be produced if the measured stellar velocity dispersions were biased high as would be the case if the BCGs (which are all selected to be strong gravitational lenses) were prolate and preferentially viewed along their major axis. However, Newman et al. (2013a,b) have argued that such a selection bias is unlikely in their sample since the distribution of BCG ellipticities appears to be typical of a randomly oriented population.

Another possible source of systematic error in the estimate of the stellar mass-to-light ratio is the assumption made by Newman et al. (2013b) that the stars in the BCG have a uniform and isotropic distribution of orbits. In their paper, they showed that mildly radial orbits would lead to an overestimate of the stellar mass-to-light ratio of 30 per cent, sufficient, in principle, to account for the discrepancy with the NFW inner DM slopes of the EAGLE clusters. We find that just such a situation is present in four of our six clusters which show radially biased orbital distributions which vary with radius in a complicated way. However, in practice, the situation is not straightforward because the mass-to-light ratio in the model of Newman et al. (2013a) is coupled to other parameters and is sensitive to the constraints on the total mass profile from lensing.

We can conclude, however, that systematic errors resulting from the assumptions made in the analysis of Newman et al. (2013b) could potentially be large enough to account for the shallow inner DM profiles that these authors infer for their clusters, in conflict with the cuspy profiles found for the EAGLE clusters. Unfortunately, it is very difficult, if not impossible, to break the degeneracies inherent in stellar kinematical analyses with existing data. High-resolution integral field spectroscopy of BCGs could prove helpful in future work.

ACKNOWLEDGEMENTS

REFERENCES

Agnello A., Evans N. W., Romanowsky A. J., Brodie J. P., 2014, MNRAS, 442, 3299
Binney J., Tremaine S., 1987, Galactic Dynamics. Princeton Univ. Press, Princeton, NJ, p. 747
Blumenthal G. R., Faber S. M., Flores R., Primack J. R., 1986, ApJ, 301, 27
Booth C. M., Schaye J., 2009, MNRAS, 398, 53
Bruzual G., Charlot S., 2003, MNRAS, 344, 1000 (BC03)
Cappellari M., 2008, MNRAS, 390, 71
Chabrier G., 2003, PASP, 115, 763
Charlot S., Fall S. M., 2000, ApJ, 539, 718
Crain R. A. et al., 2009, MNRAS, 399, 1773
Crain R. A. et al., 2015, MNRAS, 450, 1937
Dalla Vecchia C., Schaye J., 2012, MNRAS, 426, 140
Davis M., Efstathiou G., Frenk C. S., White S. D. M., 1985, ApJ, 292, 371
Di Cintio A., Brook C. B., Dutton A. A., Macciò A. V., Stinson G. S., Knebe A., 2014, MNRAS, 441, 2986
Doi M. et al., 2010, AJ, 139, 1628
Dolag K., Borgani S., Murante G., Springel V., 2009, MNRAS, 399, 497
Duffy A. R., Schaye J., Kay S. T., Vecchia C. D., Battye R. A., Booth C. M., 2010, MNRAS, 105, 2161
Durier F., Dalla Vecchia C., 2012, MNRAS, 419, 465
Dutton A. A., Macciò A. V., 2014, MNRAS, 441, 3359
Elíasdóttir Á. et al., 2007, preprint (arXiv:0710.5636)
Furlong M. et al., 2015, MNRAS, 450, 4486
Gao L., Navarro J. F., Cole S., Frenk C. S., White S. D. M., Springel V., Jenkins A., Neto A. F., 2008, MNRAS, 387, 536
Gao L., Navarro J. F., Frenk C. S., Jenkins A., Springel V., White S. D. M., 2012, MNRAS, 425, 2169
Gnedin O. Y., Kravtsov A. V., Klypin A. A., Nagai D., 2004, ApJ, 616, 16
Gnedin O. Y., Ceverino D., Gnedin N. Y., Klypin A. A., Kravtsov A. V., Levine R., Nagai D., Yepes G., 2011, preprint (arXiv:1108.5736)
Haardt F., Madau P., 2001, in Neumann D. M., Tran J. T. V., eds, Clusters of Galaxies and the High Redshift Universe Observed in X-rays. CEA, Savoie, France
Hopkins P. F., 2013, MNRAS, 428, 2840
Jenkins A., 2010, MNRAS, 403, 1859
Jenkins A., 2013, MNRAS, 434, 2094
Koopmans L. V. E. et al., 2009, ApJ, 703, L51
Laporte C. F. P., White S. D. M., 2014, preprint (arXiv:1409.1924)
Lupton R., Blanton M. R., Fekete G., Hogg D. W., O'Mullane W., Szalay A., Wherry N., 2004, PASP, 116, 133

Mamon G. A., Boué G., 2010, MNRAS, 401, 2433
Martizzi D., Teyssier R., Moore B., Wentz T., 2012, MNRAS, 422, 3081
Moster B. P., Naab T., White S. D. M., 2013, MNRAS, 428, 3121
Navarro J. F., Eke V. R., Frenk C. S., 1996a, MNRAS, 283, L72
Navarro J. F., Frenk C. S., White S. D. M., 1996b, ApJ, 462, 563
Navarro J. F., Frenk C. S., White S. D. M., 1997, ApJ, 490, 493
Navarro J. F. et al., 2004, MNRAS, 349, 1039
Navarro J. F. et al., 2010, MNRAS, 402, 21
Neto A. F. et al., 2007, MNRAS, 381, 1450
Newman A. B., Treu T., Ellis R. S., Sand D. J., Nipoti C., Richard J., Jullo E., 2013a, ApJ, 765, 24
Newman A. B., Treu T., Ellis R. S., Sand D. J., 2013b, ApJ, 765, 25
Okabe N., Smith G. P., Umetsu K., Takada M., Futamase T., 2013, ApJ, 769, L35
Okamoto T., Shimizu I., Yoshida N., 2014, PASJ, 66, 70
Planck Collaboration XVI, 2014, A&A, 571, A16
Pointecouteau E., Arnaud M., Pratt G. W., 2005, A&A, 435, 1
Pontzen A., Governato F., 2012, MNRAS, 421, 3464
Pontzen A., Governato F., 2014, Nature, 506, 171
Portinari L., Chiosi C., Bressan A., 1998, A&A, 334, 505
Power C., Navarro J. F., Jenkins A., Frenk C. S., White S. D. M., Springel V., Stadel J., Quinn T., 2003, MNRAS, 338, 14
Read J. I., Gilmore G., 2005, MNRAS, 356, 107
Rocha M., Peter A. H. G., Bullock J. S., Kaplinghat M., Garrison-Kimmel S., Oñorbe J., Moustakas L. A., 2013, MNRAS, 430, 81
Rosas-Guevara Y. M. et al., 2013, preprint (arXiv:1312.0598)
Sand D. J., Treu T., Smith G. P., Ellis R. S., 2004, ApJ, 604, 88

Scannapieco C. et al., 2012, MNRAS, 423, 1726
Schaller M. et al., 2015, MNRAS, 451, 5765
Schaye J., 2004, ApJ, 609, 667
Schaye J., Dalla Vecchia C., 2008, MNRAS, 383, 1210
Schaye J. et al., 2010, MNRAS, 402, 1536
Schaye J. et al., 2015, MNRAS, 446, 521
Spergel D. N., Steinhardt P. J., 2000, Phys. Rev. Lett., 84, 3760
Springel V., 2005, MNRAS, 364, 1105
Springel V., White S. D. M., Tormen G., Kauffmann G., 2001, MNRAS, 328, 726
Strigari L. E., Frenk C. S., White S. D. M., 2010, MNRAS, 408, 2364
Strigari L. E., Frenk C. S., White S. D. M., 2014, preprint (arXiv:1406.6079)
Trayford J. W. et al., 2015, preprint (arXiv:1504.04374)
Tremonti C. A. et al., 2004, ApJ, 613, 898
Umetsu K. et al., 2014, ApJ, 795, 163
Vikhlinin A., Kravtsov A., Forman W., Jones C., Markevitch M., Murray S. S., Van Speybroeck L., 2006, ApJ, 640, 691
Vogelsberger M., Zavala J., Loeb A., 2012, MNRAS, 423, 3740
Vogelsberger M. et al., 2014, Nature, 509, 177
Walker M. G., Penarrubia J., 2011, ApJ, 742, 20
Wiersma R. P. C., Schaye J., Smith B. D., 2009a, MNRAS, 393, 99
Wiersma R. P. C., Schaye J., Theuns T., Dalla Vecchia C., Tornatore L., 2009b, MNRAS, 399, 574

This paper has been typeset from a TEX/LATEX file prepared by the author.